Brodogradnja Volume 77 Number 3 (2026) 77301

journal homepage: www.brodogradnja.fsb.hr

Brodogradnja

An International Journal of Naval Architecture and Ocean Engineering for Research and Development

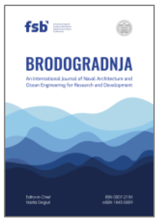

Fault diagnosis and restoration of ship structure monitoring signals based on machine learning

Haoyun Tang[1,*], *Bangchao Fu*[1], *Haiyang Guan*[1], *Ying Yang*[1], *Qian Wan*[2,3]

[1] *Navigation College, Dalian Maritime University, Dalian 116026, China*
[2] *College of Shipbuilding Engineering, Harbin Engineering University, Harbin 150001, China*
[3] *Dalian shipbuilding industry Co., Ltd, Dalian 116026, China*

ARTICLE INFO

Keywords:
Ship structure
Artificial neural network
Fault diagnosis
Signal restoration

ABSTRACT

To prevent signal faults from causing misjudgements of structural health and even catastrophic accidents in ship monitoring systems, a fault diagnosis and restoration method is proposed by using machine learning. The method integrates advanced technologies including wavelet transform, IPSO-BP neural network, CNN, event-triggered sampling based on predictive zero-crossing instant, and adaptive segmented least squares algorithm, focusing on efficient identification and rectification of the typical signal faults. Based on the monitoring data of a model test, an impact analysis on the fault diagnosis and restoration method is carried out, covering aspects like noise resistance, fault severity, fault occurrence time, and ship monitoring position. The result indicates that the proposed method has a total diagnostic rate of no less than 98 % at different monitoring positions, and its noise-resistance ability is superior to that of the LSTM and Random Forest algorithms. Moreover, it delivers outstanding restoration effects. Compared to traditional mean segmentation, it reduces RMSE by 73.86 % for bias faults, 75.49 % for drift faults, and 19.55 % for impulse faults. This method can effectively enhance the stability of ship structural health monitoring systems, providing critical technical support for intelligent ship navigation safety.

1. Introduction

To prevent the collapse of hull structures caused by some imperceptible damages, the real-time structural health monitoring has become an indispensable function in intelligent ship's systems [1-4]. However, actual ship tests have revealed that the long-term operation of ship structural monitoring systems still face significant challenges. Currently, most ship structural health monitoring systems rely heavily on the structural response data provided by contact-type sensors [5-7]. These sensors are distributed at various key parts and are responsible for collecting important data such as stress, strain, and vibration, providing crucial evidence for assessing the structural health. However, the hull internal environment is extremely harsh, characterized by the coexistence of high temperature, high humidity, strong vibration, and corrosive gases, which pose severe challenges to the normal operation of the sensors. In such an environment, sensors are prone to malfunctions,

* Corresponding author.
E-mail address: conanthy@126.com

https://doi.org/10.21278/brod77301
Received 30 May 2025; Received in revised form 16 November 2025; Accepted 26 November 2025
Available online 3 December 2025
ISSN 0007-215X; eISSN 1845-5859

such as aging of sensor components and loosening or damage of connecting wires. According to relevant statistical data [8], the annual failure rate of sensors in the harsh hull environment is as high as 15 % - 20 %. When monitoring sensors malfunction, the ship monitoring system will be unable to accurately reflect the real state of the current hull structure. The data collected by faulty sensors may have deviations, missing values, or even errors. These abnormal data will be transmitted to the monitoring system, leading to deviations in the system's judgment on the health status of the hull structure. More seriously, certain fault characteristics present in the monitoring signals, such as abnormal pulse signals and unstable fluctuations, may trigger the alarm mechanism of the monitoring system, causing false alarms. These false alarms not only interfere with the normal judgment of the crew, but also may lead to unnecessary emergency responses, resulting in the waste of time and resources. Furthermore, the monitoring deviations caused by these faults pose more serious safety risks to the navigation of intelligent ships. Based on inaccurate monitoring data, potential damages may fail to be detected in a timely manner, finally leading to the failure of the ship structure [9-12]. Therefore, it is abundantly clear that the research on fault diagnosis and restoration technology for ship structure monitoring signals is of utmost necessity. This technology is crucial for ensuring the reliable operation of ship monitoring systems, safeguarding the safety of ships and personnel during navigation.

Monitoring signal diagnosis and restoration technology is an interdisciplinary research field that integrates knowledge from multiple disciplines such as data analysis, signal processing, decision-making, and artificial intelligence [13,14]. Currently, this technology implementation is mainly based on two main methodologies: analytical model-based approaches and data-driven methods. The core of the analytical model lies in diagnosing faults according to the deviations between the analytical solutions and the actual measured values. Ding and Guo [15] had developed a diagnosis analytical model that integrate residuals with threshold settings for time-domain monitoring signals, while Tan et al. [16] had combined the diagnosis analytical model with a Kalman filter to identify fault parameters in sensors. Although these diagnostic analytical models can detect faults relatively quickly, they often encounter difficulties in applications due to their limited resistance to signal interference. But for data-driven methods, their advantages such as strong anti-interference ability, adaptability to complex working conditions, and the dispensability of precise mathematical modeling led to an upsurge in the field of fault diagnosis and restoration. In order to deal with different signal characteristics, the data-driven methods often incorporate multiple intelligent algorithms, including expert systems and artificial neural networks [17-19]. Jiang [20] achieved the fault diagnosis of fiber optic sensors by combining support vector machine (SVM) with random forest (RF) algorithm. A hybrid data-driven model based on the multiple echo state network was proposed by Li et al. [21] to enhance the accuracy and robustness of fault diagnosis in high-voltage circuit breakers, while Ma et al. [22] developed a fault diagnosis hybrid model by integrating improved particle swarm optimization (IPSO), variational mode decomposition (VMD) and support vector machine. Then, Huang et al. [23] developed a Barabási-albert model-enhanced genetic algorithm for improving the fault diagnosis of ship power grid. However, despite the extensive research and application of signal diagnosis and restoration technologies in crucial equipment such as high-voltage circuit breakers, power systems, and marine engines, there is a notable scarcity of investigations of these technologies in the realm of structural monitoring with intelligent ships at its core. In fact, in contrast to the stable environment of these local equipment, the marine environment in which intelligent ships sail is intricate and highly variable. Under the impact of waves, the ship's hull structure generates a complex mixture of high and low-frequency responses that are difficult to fully comprehend. This complexity poses a significant hurdle, making it arduous to directly apply traditional signal diagnosis and restoration techniques to ship structural health monitoring. Consequently, it is of pressing necessity to initiate the research of fault diagnosis and restoration technologies that focus on the monitoring signals of ship structures.

In the research, an adaptive method of signal diagnosis and restoration is investigated for typical faults that often occur in ship monitoring sensors. To tackle the challenge of insignificant fault signal characteristics in hull structural monitoring, this research proposes an intelligent event-triggered sampling mechanism. This mechanism integrates signal cross-validation strategy, improved particle swarm optimization and Back-Propagation (BP) neural networks to effectively extract the features of monitoring data at the predicted zero-crossing instant and determine the signal restoration junctions. Then, by combining the event-triggered sampling with the wavelet transform, the research also constructs a multidimensional input of monitoring signal characteristics and uses Convolutional Neural Networks (CNN) as the core architecture for signal fault diagnosis. Subsequently, for identified faulty signals, the research develops an adaptive segment least squares algorithm to eliminate the impact of wrong signal fluctuations at the truncation location.

The innovativeness of this research primarily lies in the development of a zero-crossing instant sampling algorithm founded on the IPSO-BP and event-triggered mechanism for signal diagnosis and restoration. This algorithm is ingeniously integrated with techniques including CNN feature recognition and least-squares segmented restoration. Consequently, during fault diagnosis, it can effectively accentuate fault characteristics. Meanwhile, in the process of signal restoration, it is capable of pinpointing time points with minimal errors for truncation and rectification. This novel algorithm endows the entire signal diagnosis and restoration process with the capabilities of autonomously enhancing fault identification and searching for optimal restoration positions. Therefore, this research not only facilitates the progress of signal diagnosis and restoration within the maritime industry but also lays the foundation for reliable ship structural health monitoring. Moreover, it ultimately offers technical support for smart shipping and maritime safety.

2. Materials and methods

2.1 Fault types of structural monitoring signals

According to the characteristics of sensor faults observed during long-term monitoring of actual and large-scale ships [24-26], the faults in ship structural monitoring signals can be categorized into two types: soft faults and hard faults. Herein, soft faults occur when the data transmission of the monitoring sensor is not interrupted, but the sensor's fundamental parameters change over time due to prolonged monitoring attrition, leading to variations in the monitored data. The signal characteristics of soft faults typically manifest as small amplitude changes and slow variations, such as signal drift. On the other hand, hard faults arise when the sensor suffers physical damage or poor contact during long-term monitoring. The signal characteristics of hard faults are marked by large amplitude changes and high fluctuation kurtosis, including phenomena such as signal deviation, instantaneous impulses, and interruptions.

In the ship structural monitoring, assuming that the monitoring signal varying over time is denoted as $\bar{M}\left(t\right)$, the relationship between the monitored data and the true data can be expressed as:

$$\bar{M}(t) = \gamma M(t) + \varepsilon(t) \tag{1}$$

where t represents the signal monitoring time; $M(t)$ represents the true data; $\varepsilon(t)$ is the signal interference coefficient; γ is the signal extension coefficient. Incorporating the characteristics of sensor faults, the fault signals can be categorized into four typical failures: bias, drift, impulse, and open-circuit. The mathematical models for these faults are presented in Table 1.

Table1 Mathematical models of typical signal faults

Fault Type	Mathematical Model
Bias	$\varepsilon(t) = \lambda \times \mathrm{H}(t - t^*)$; $\gamma = 1$
Drift	$\varepsilon(t) = \upsilon \times (t - t^*) \times \mathrm{H}(t - t^*)$; $\gamma = 1$
Impulse	$\varepsilon(t) = \sigma \times \Gamma\left[(t + \Delta t) - t^*\right] - \sigma \times \Gamma\left[(t - \Delta t) - t^*\right]$; $\gamma = 1$
Open-circuit	$\varepsilon(t) = \gamma = 0$

Herein, t^* represents the fault occurrence time; Δt is the sample time; λ is the bias amplitude; υ is the drift slop; γ is the open-circuit coefficient; σ is the impulse magnitude. $\mathrm{H}(t)$ is Heaviside function, and $\Gamma(t)$ is unit impulse function, respectively.

2.2 Wavelet transform decomposition

The extraction of detailed characteristics from monitoring signals is a crucial element in the identification of fault signals. Wavelet decomposition, as a significant signal processing technique, provides substantial advantages in the extraction of signal details. This research adopts a fast algorithm for wavelet decomposition, known as the multi-resolution analysis (MRA), which can mine the detailed characteristics of signal faults by obtaining the signal fluctuation characteristics of correlation coefficients at different scales. In the MRA, the structural monitoring signal space is decomposed into a series of subspaces V and orthogonal complement spaces W:

$$V_0 = V_1 \oplus W_1 = \cdots = V_{J'-1} \oplus W_1 \oplus W_2 \cdots \oplus W_{k'} \cdots \oplus W_{J'-1} \tag{2}$$

The signal function in the space is transformed using the multi-resolution analysis:

$$f_0(t) = \sum_{m'} c_{j',m'} \varphi_{j',m'}(t) + \sum_{k'}^{J'-1} \sum_{m'} d_{j',m'} \phi_{j',m'}(t) \tag{3}$$

where $\varphi_{j',m'}$ and $\phi_{j',m'}$ are the standard orthogonal bases of the spaces V and W, respectively; the scale expansion coefficients $c_{j',m'}$ and the wavelet expansion coefficients $d_{j',m'}$ can be obtained iteratively according to the low-pass filter weight function h and the high-pass filter weight function g:

$$c_{j',m'} = \sum_{k'} h(k' - 2m') c_{j'-1,m'} \tag{4}$$

$$d_{j',m'} = \sum_{k} g(k' - 2m') c_{j'-1,m'} \tag{5}$$

In addition, combining the two-scale equation and the orthogonality of the wavelet basis function, there is also a relationship between the scale expansion coefficients and the wavelet expansion coefficients at any scale:

$$c_{j'-1,m'} = \sum_{k'} c_{j',k'} h(m' - 2k') + \sum_{k'} d_{j',k'} g(m' - 2k') \tag{6}$$

Finally, the monitoring signal is decomposed into a series of approximate coefficients Ca(n*) and detail coefficients Cd(n*), which will become a part of the multi-dimensional input in the subsequent artificial neural network. Figure 1 show the specific process of the wavelet transform decomposition.

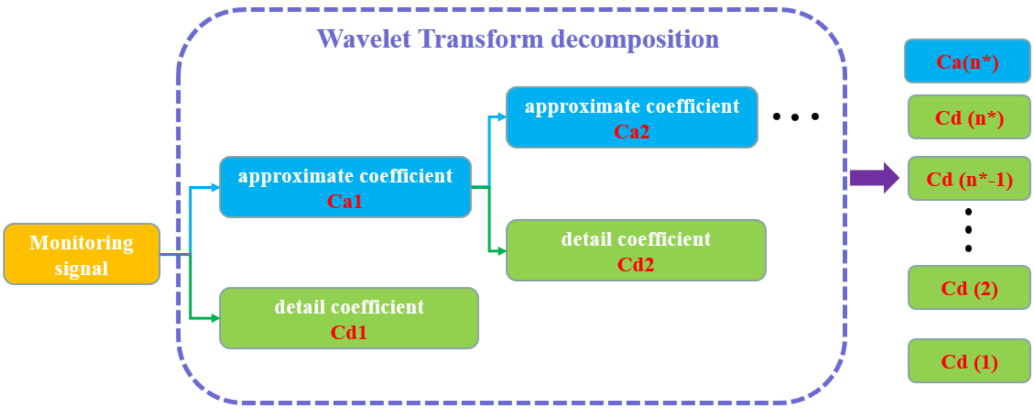

Fig. 1 Wavelet transform decomposition

2.3 Event-triggered sampling based on predictive zero-crossing instant

To effectively enhance the identification of signal fault characteristics, this research combines the optimized particle swarm algorithm, back-propagation neural network, and an event-triggering mechanism to construct an intelligent event-triggered sampling mechanism. This mechanism, based on artificial neural network prediction, can autonomously search for critical instants and extract the signal characteristics.

2.3.1 Event-triggered Sampling

In ship structure monitoring, the range of sampling frequency at various monitoring positions is often from 50 to 1000 Hz. Although this high sampling frequency provides sufficient information for characterizing the hull structural status, the enormous amount of data and the interference of multiple noise signals in the signal data also impose a significant burden on the onboard computer, reducing the timeliness of hull structural damage warnings. To improve the response speed of the monitoring system, event-based triggered sampling is adopted. In the event-triggering mechanism, the sampling time t_{k+1} can be expressed as:

$$t_{k+1} = t_k + \Delta t_k \tag{7}$$

where t_k is the time of the k-th sample, and Δt_k is the time interval between the k-th and (k+1)-th samples, determined by the event-triggering conditions, which are also represented as:

$$\Delta t_k = \begin{cases} t - t_k, & \text{if} \left| y_P(t) - y_{ref} \right| \le \varepsilon \\ \infty, & \text{otherwise} \end{cases} \tag{8}$$

Herein, the reference y_{ref} and deigned threshold ε both are set to zero in the study to search the zero-crossing instants. The triggering of events mainly depends on the predicted signal y_P, which is obtained using the IPSO-BP neural network. Unlike the traditional triggering condition based on a fixed threshold, the IPSO-BP prediction-based triggering mechanism is adaptive and independent of human factors. This approach can effectively reduce the data volume while further enhancing the system's ability to autonomously extract the fluctuation characteristics from the ship monitoring signals.

2.3.2 IPSO-BP neural network.

In the intelligent sampling mechanism, IPSO-BP neural networks serve the purpose of searching for the temporal positions of signal features. For the BP neural network, a series of neurons, such as X_m, K_i, and Y_j (m=1, 2, ⋯M; i=1, 2, ⋯I; j=1, 2, ⋯J), are arranged in the three numerical layers, which are input layer, hidden layer and output layer, as shown in Figure 2. The linear transfer functions (TF^I and TF^{II}) and sigmoid function (SF) are used to connect and activate these neurons:

$$TF_n^I(x) = \omega_{mi,n}^I x + b_{i,n}^I \tag{9}$$

$$TF_n^{II}(x) = \omega_{ij,n}^{II} x + b_{j,n}^{II} \tag{10}$$

$$SF(x) = \frac{1}{1+e^x} \tag{11}$$

Herein, these transfer functions' weights ($\omega_{mi,n}^I$, $b_{i,n}^I$, $\omega_{ij,n}^{II}$, $b_{j,n}^{II}$) are progressively determined through iterative computations during the BP training. In order to find the optimal values for these weights, the BP training takes forward propagation phase and backward propagation phase.

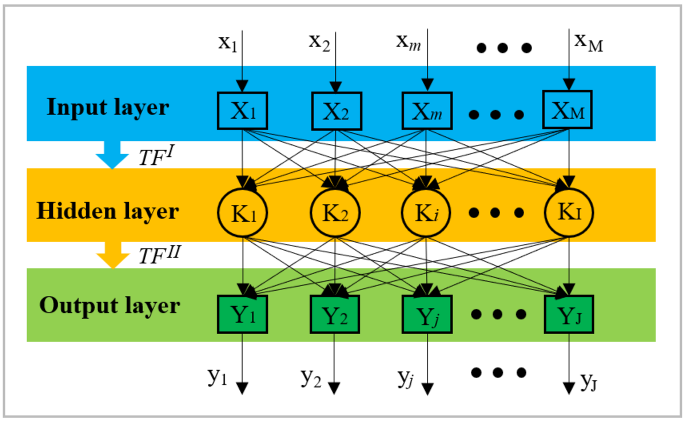

Fig. 2 BP neural network framework

In the forward propagation phase, a series of signal inputs x_m derived from several monitoring positions is applied. Each neuron in the BP network processes the incoming information by applying the transfer functions to the weighted sum of its inputs. Additionally, the sigmoid function is also used to activates the BP network's nonlinearity for learning complex patterns. The output of this phase is the predicted signal value y_j generated by the BP network based on the current set of weights, and it is further compared with the expectation d_j to calculate the error at the n-th iterative calculation:

$$e(n)=\frac{1}{2}\sum_{j=1}^{J}\left[y_j(n)-d_j\right]^2 \tag{12}$$

For the backward propagation phase, the goal is to minimize the error by adjusting the weights using the steepest gradient descent algorithm. This calculation process is repeated iteratively, with the weights being updated incrementally in each iteration until the error is reduced to an acceptable level. The n-th adjustment on the weights are shown as follows:

$$\Delta\omega_{mi,n}^{I}=-\eta\frac{\partial e(n)}{\partial x_i(n)}x_m(n) \tag{13}$$

$$\Delta\omega_{ij,n}^{II}=-\eta\frac{\partial e(n)}{\partial\omega_{ij}^{II}(n)} \tag{14}$$

$$\Delta b_{j,n}^{I}=\eta k_i(1-k_i)x_m\sum_{m=1}^{M}\omega_{mi}^{I}(n)e(n) \tag{15}$$

$$\Delta b_{i,n}^{II}=-\eta\frac{\partial e(n)}{\partial b_i(n)} \tag{16}$$

In the BP neural network, the determination on hyperparameters remains a challenge that heavily relies on technician experience. This reliance on manual selection can introduce subjectivity and may not always lead to the optimal starting point for the network's training. To enhance the performance of the BP neural network, the research introduces an improved particle swarm optimization. This sophisticated optimization technique is designed to find the most suitable set of hyperparameters for the neural network, including the initial weights, learning rates. In the IPSO, the position of each particle represents a variable in the optimization problem, and the particles explore the solution space iteratively based on their objective function. During each iteration, each particle updates its position by taking into account the best position it has experienced so far (known as the personal best p_i) and the best position found by the entire swarm (known as the global best p_g). This process allows the particles to move towards more promising regions of the search space. Additionally, each particle uses a fitness function to evaluate whether its current position is optimal. In the iterative process, the velocity v and position z of the i-th particle are updated according to the following equations:

$$v_i\left(t^*+1\right)=\gamma_p v_i\left(t^*\right)+c_1 r_1\left(t^*\right)\left[p_i\left(t^*\right)-z_i\left(t^*\right)\right]+c_2 r_2\left(t^*\right)\left[p_g\left(t^*\right)-z_i\left(t^*\right)\right] \tag{17}$$

$$z_i\left(t^*+1\right)=z_i\left(t^*\right)+v_i\left(t^*+1\right) \tag{18}$$

where r_1 and r_2 are uniform random numbers in the range [0,1] to enhance the randomness of particle search. c_1 and c_2 are the IPSO learning factors, respectively. γ_p represents the inertia weight, which plays a crucial role in balancing the algorithm's global search capability and local search capability. Unlike the traditional PSO, where the inertia weight is set as a constant, the IPSO algorithm establishes a dynamically adjusted inertia weight to enhance the search capability of the particle swarm:

$$\gamma_p=\begin{cases}\gamma_{p,\min}-\dfrac{\left(\gamma_{p,\max}-\gamma_{p,\min}\right)\left(\chi-\chi_{\min}\right)}{\chi_{avg}-\chi_{\min}} & \chi\le\chi_{avg}\\ \gamma_{p,\max} & \chi>\chi_{avg}\end{cases} \tag{19}$$

where χ is the real-time particle fitness; $\gamma_{p,\max}$ and $\gamma_{p,\min}$ are the maximum and minimum of the inertia weights. χ_{avg} and $\chi_{\min}$ denote the average and minimum particle fitness, respectively. The integration of IPSO with the BP neural network brings significant improvements in convergence speed, prediction accuracy, robustness, and global search capability. These enhancements make the IPSO-BP neural network more effective and reliable for a wide range of applications, particularly in complex and dynamic environments where traditional artificial neural networks (ANNs) may struggle to perform optimally. Finally, the IPSO-BP neural network will be able to effectively predict the zero-crossing instant, thereby triggering an event mechanism to enable the sampling of monitoring signals at critical moments.

2.4 Convolutional neural network

In the diagnosis of monitoring signal faults, the research uses a numerical model based on Convolutional Neural Networks, which can offer several advantages. CNNs excel in hierarchical feature learning, enabling them to automatically extract complex patterns and features from the monitoring signals. Their local connectivity and parameter sharing can also reduce the number of parameters, making the network more efficient and easier to train, especially with large datasets. Additionally, CNNs possess translation invariance, allowing them to diagnosis patterns regardless of their position in the signal, which is crucial for accurate fault detection. Furthermore, CNNs are inherently robust to noise and variations in the data, ensuring reliable performance even in less-than-ideal conditions.

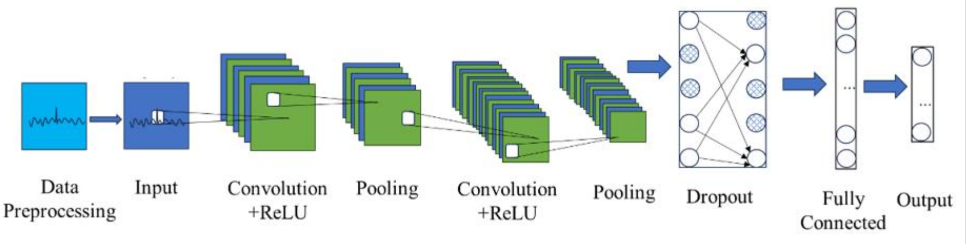

Fig. 3 CNN architecture

The CNN architecture for signal fault diagnosis consists of several components, which are input layer, convolutional layer, pooling layer, fully connected layers and output layer, as shown in Figure 3. Herein, input Layer is used to receives the multidimensional signal data based on wavelet transform decomposition and event-triggered sampling. In convolutional layer, a set of learnable filters is applied and expressed as:

$$\varphi_j^l = f\left(\sum_{i=1}^{N_{l-1}} \varphi_i^{l-1} * \lambda_{ij}^l + \zeta_j^l\right) \tag{20}$$

where φ_j^l is the output of the j-th filter in the l-th layer. φ_i^{l-1} is the input from the (l−1)-th layer. λ_{ij}^l is the i-th filter in the l-th layer. ζ_j^l is the bias term. f is the activation function, which is the Rectified Linear Unit (ReLU) in the research. This function replaces all negative values in the feature map with zero, allowing the network to learn complex patterns and relationships in the data. In the CNN, the pooling layer is used to reduce the spatial dimensions of the feature maps, thereby reducing the computational complexity. The max pooling algorithm are applied and expressed as:

$$\varphi_j^l = \max(\varphi_i^{l-1}) \tag{21}$$

Max pooling can divide the feature map into small regions and outputs the maximum value from each region, capturing the most salient features. To prevent overfitting, the research also adopts a regularization technique by randomly deactivating a fraction of neurons. In dropout layer, a certain percentage of neurons temporarily removed from the CNN network, along with their incoming and outgoing connections. For a given neuron ψ_i, the output of the neuron is scaled by the dropout rate p as follows:

$$\psi_{i'} = \begin{cases} 0 & \text{with probability } P_S \\ \dfrac{\psi_i}{1-P_S} & \text{otherwise} \end{cases} \tag{22}$$

By promoting redundancy and preventing the network from memorizing the training data, the dropout helps the network generalize better to unseen data. The high-level features extracted by the pooling and dropout layers are fed into a fully connected layer to perform the final fault classification. The output of this fully connected layer is a probability distribution over the possible fault classes:

$$\Phi = \mathrm{softmax}(W\varphi + \zeta) \tag{23}$$

Finally, the signal fault diagnosis is provided in the output Layer, according to the calculated probability distribution. The CNNs have powerful feature extraction and classification capabilities. By learning hierarchical representations of the input signals and adapting to the unique characteristics of the signal faults, CNNs provide an efficient approach to detecting and diagnosing faults in complex signal fluctuations.

2.5 Adaptive segment least squares method

Signal restoration is a critical process in the field of hull structural health monitoring. The goal is to recover the original signal from a corrupted or incomplete version. This is particularly challenging when the signal is affected by noise, interference, or missing part data. For signal restoration, the Least Squares (LS) method is widely used by minimizing the sum of the squares of the differences between the observed data and the estimated signal. However, due to the complexity and variability of actual marine environment, the monitored signals during ship navigation often have long-term irregularities, which reduces the accuracy and smoothness of the signal restoration based on LS. Therefore, this research introduces an adaptive segment least squares (ASLS) method based on the zero-crossing instants. The ASLS divides the monitoring signal into multiple segments and applies least squares fit to each segment individually. The length of each segment is automatically adjusted, according to the local fluctuation characteristics of IPSO-BP signal prediction. The corrected signal $\hat{s}$ after ASLS restoration is expressed as:

$$\hat{s}(t) = \begin{cases} s(t) & \text{if } t \notin \text{faulty segment} \\ s(t) - (\hat{\alpha}_q t + \hat{\beta}_q) & \text{if } t \in \text{faulty segment} \end{cases} \tag{24}$$

where Q is the number of signal segments. $\hat{\alpha}_q$ and $\hat{\beta}_q$ are the slope and intercept obtained by the least squares method for the q-th segment, respectively. When a monitoring sensor fault occurs, the fault duration of the signal is searched for zero-crossing instants, and these instants are used as boundaries to perform autonomous segmentation. Within each segment, the faulty signal is finally corrected using the least squares method.

3. Verification and analysis of signal fault diagnosis

3.1 Establishment of signal feature multidimensional input

In ship structure monitoring, the signals collected by sensors are often a fusion of various factors, making the detailed features of signal faults less prominent. Therefore, a multi-dimensional input is adopted in the signal fault identification model. This multi-dimensional input involves integrating methods such as wavelet decomposition and the event-driven sampling based on predictive zero-crossing instant, which make signal fault identification model effectively distinguish the difference in varied signal faults.

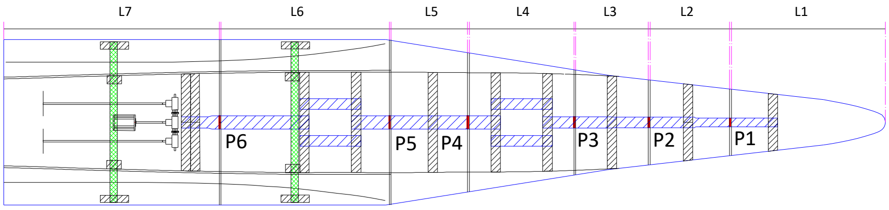

Fig. 4 Trimaran monitoring layout

To demonstrate the feasibility of signal fault diagnosis and restoration, the monitoring data were used from the experiment of a trimaran model [6]. Figure 4 shows the monitoring layout on the trimaran model. The trimaran model's length and width are 5.7 and 1.1 m, and it also has a design draft of 0.2 m. The model is divided into seven segments (L1 to L7) along its length, and the longitudinal stiffness distribution of the hull structure is simulated by fixing longitudinal beams with varying cross-sections. When the ship model is sailing in waves, these longitudinal beams suffer vertical deformation due to the uneven hydrodynamic pressure as it rises and falls with the waves. Through the arrangement of strain gauges on the longitudinal beams at segmented locations, the dynamic strain is recorded. Subsequently, through a beam calibration experiment that establishes a linear relationship between the vertical bending moment (VBM) and the strain, the fluctuation of the vertical bending moment can ultimately be obtained by further analyzing the data from the established relationship. In this study, the fluctuations of the vertical bending moment at different sectional positions are regarded as the monitoring signals of the ship's simplified structure [27-29]. Figure 5 shows the time history of the structural response signals monitored at six positions (P1 to P6) from the bow to the stern of the trimaran under irregular waves (significant wave height: 2.2 m; characteristic period: 7.5 s). In the model test, the sampling frequency of the monitoring signals was 100 Hz, and the effective monitoring period was 200 s.

The research develops a multi-signal cross-validation strategy for diagnosing the monitoring signals at various positions. In the multi-signal cross-validation, the monitoring signals from all positions except the target signal are used as inputs in the IPSO-BP neural network. Within the IPSO-BP neural network framework, the input layer consists of 5 neurons, the hidden layer contains 5 neurons, and the output layer has 1 neuron. This IPSO is designed to find the most suitable set of hyperparameters for the BP neural network, including the initial weights, learning rates. Herein, a particle population of 50 is configured, and the particle swarm has a dimension of 36. The position of every particle is confined to the interval of [-2, 2], and the velocity of each particle varies from -0.5 to 0.5. After the ANN's training, the time-domain prediction on the target monitoring position can be achieved. The input-output relationship for the cross-validation of ship monitoring signals is illustrated in Figure 6. For instance, when the fault diagnosis is taken on the monitoring signal at the stern position (P6), the IPSO-BP neural network is trained using the signals from P1 to P5 as inputs. The data from 0 to 120 s are used as cross-validation area for the IPSO-BP neural network's training. Once the IPSO-BP training is complete, the signals from P1 to P5 at the subsequent time (120-200 s) can be fed into the IPSO-BP neural network to predict and diagnose the stern monitoring signal. Similarly, this same training process is applied respectively to predict and diagnose the target signals from P1 to P5, using the corresponding signals from the other monitoring positions as inputs.

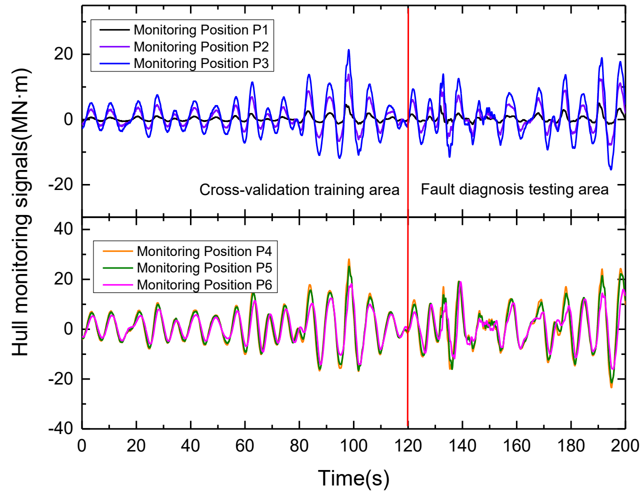

Fig. 5 Hull mmonitoring signal at different positions

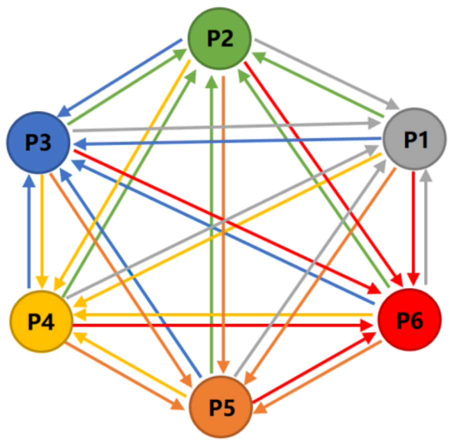

Fig. 6 Input-output relationship for the cross-validation of ship monitoring signals

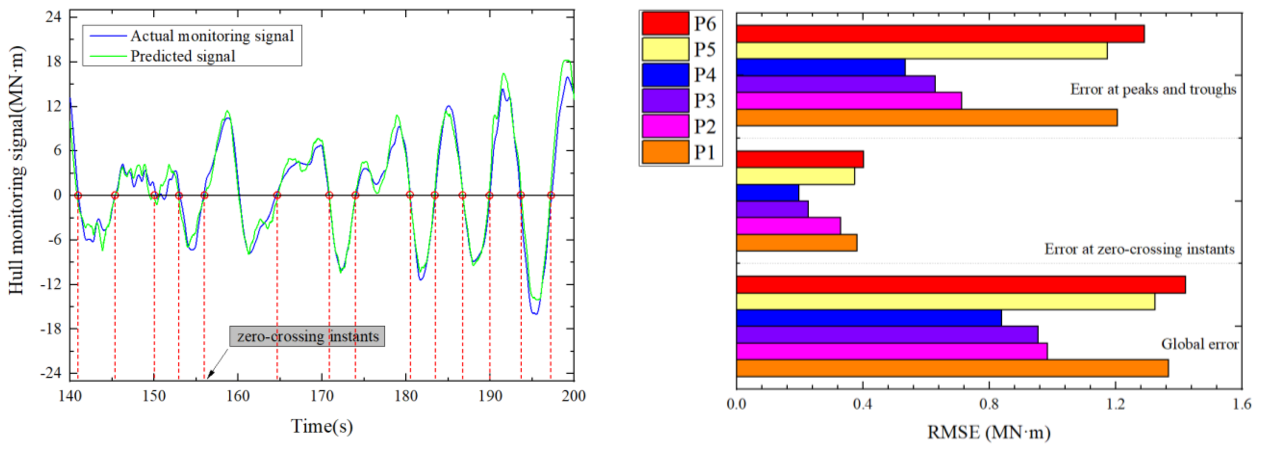

(a) Search for zero-crossing instants (b) Error comparison

Fig. 7 Comparison between original monitoring signal and predicted signal

Figure 7(a) compares the actual stern monitoring signal with the IPSO-BP predicted signal. The root mean square error (RMSE) between the actual and predicted signals is 1.42MN·m, which indicates a high level of accuracy. The results demonstrate that the IPSO-BP neural network can capture the trend of signal fluctuations effectively under the cross-validation strategy. Although there are some discrepancies in the peaks and troughs, the predictions at the zero-crossing instants are relatively accurate. For all monitoring positions, the errors at zero-crossing instants are much smaller than the global error and the error at peaks and troughs, as shown in Figure 7(b). This can be attributed to the fact that the zero values of hull structural responses always occur when the ship is in the state of buoyancy equilibrium. Consequently, the signals at these zero-crossing instants are correlated, making it easier to diagnose and restoration the signals based on this common bench mark.

Considering the complex high-frequency vibrations generated by the stern propellers and the harsh operational environment in the hull stern [30], it is assumed that the occurrence of a single typical fault at the stern monitoring position (P6) and the four types of signal fault are simulated using the fault model in Table1. To analyze these fault signal features, a 5-level wavelet decomposition is carried out, using the sym8 wavelet function as the basis. The event-triggered sampling based on predictive zero-crossing instant is also taken, and the slope based on the data of the event-driven sampling is calculated. Figure 8 shows the signal feature extraction of the raw monitoring signal at stern.

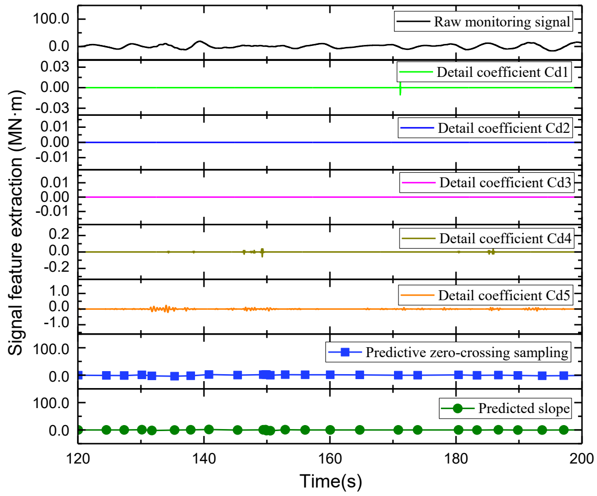

Fig. 8 Signal feature extraction of the raw monitoring signal at stern

The signal feature extraction of the stern monitoring signal under different typical faults are also given, as shown in Figure 9. Herein, the signal faults are added respectively: a bias fault at 140 s with an amplitude of 160, a drift fault at 150 s with a slope of 2.2, an impulse fault at 160 s with an amplitude of 150, and an open-circuit fault at 145 s. Obviously, when a signal fault occurs, the detail coefficients have significant fluctuations at the fault moment, particularly for the Cd2 and Cd3 coefficients. The synchronized fluctuations of these detail coefficients can trigger the fault identification mechanism, thereby initiating the detection and classification of signal faults. In addition, the data of the intelligent event-driven sampling and its calculated slopes also show different fluctuation characteristics. These distinct data acquisition characteristics of fault signals will provide the basis for fault identification. Finally, the multidimensional input for signal diagnose includes the detail coefficients (Cd1-Cd5), the data of the intelligent event-driven sampling and its calculated slopes.

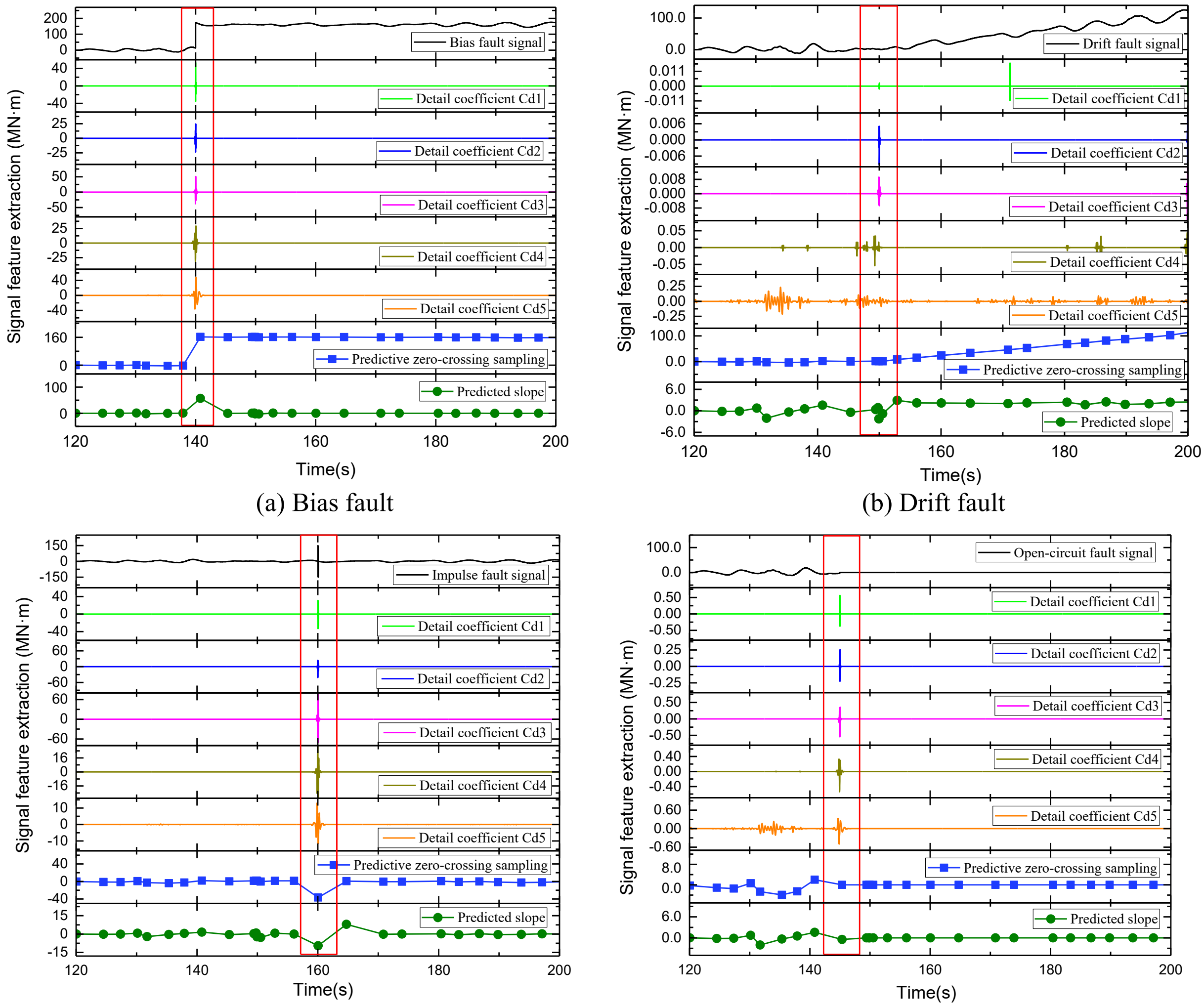

(a) Bias fault (b) Drift fault

(c) Impulse fault (d) Open-circuit fault

Fig. 9 Signal feature extraction under different typical faults

3.2 Training and testing of diagnostic model

In the research, a numerical diagnosis model based on CNN and the multidimensional input of signal feature extraction is established to automatically identify signal faults, as shown in Figure 10. The judgment basis of the fault diagnosis model focuses on local input data segments. To cover the fault characteristics in different time periods, the diagnosis model gradually traverses the entire time-series data through the mechanism of the sliding window with a fixed time length. During the sliding process, the valid input data of a fixed duration is intercepted. Therefore, the variation in the overall data volume will not affect the core structure and judgment logic of the fault diagnosis model. The monitoring data is transformed into a multi-dimensional matrix as the input for the CNN. This matrix includes the sample length, the number of characteristic signals, and the slip mark. Here, the sample length refers to the number of sample data within a fixed time length. The characteristic signals consist of wavelet coefficients Cd1-Cd5, event-triggered sampled data, and the calculated slopes. The slip mark represents the number of times the numerical extraction window slips.

To simulate the random triggering mechanism of sensor faults, this research constructs a signal sample set at different times, which the signal fluctuation and fault construction are selected randomly in the fault diagnosis testing area (120-200 s). The relevant parameters for typical faults are also randomly selected within the specified range ($\lambda \in [2.5, 180.0]$; $\upsilon \in [0.4, 4.5]$; $\sigma \in [4.0, 180.0]$).The sample includes one normal signal category and four fault signal categories, and each category contains 33 signal fluctuation subsamples that contain the data within 2 s. The signal categories are labeled with roman numerical identifiers as follows: I for normal signals; II for bias signals; III for drift signals; IV for impulse signals; and V for open-circuit signals.

For each signal category, 22 subsamples are selected for CNN training and 11 subsamples are reserved for signal fault diagnosis test. A total of 110 signal fluctuation subsamples and their corresponding label data are imported into the CNN diagnosis model for training. Before the CNN training, the training data are normalized and randomly shuffled to avoid any potential influence of the data order on the training process.

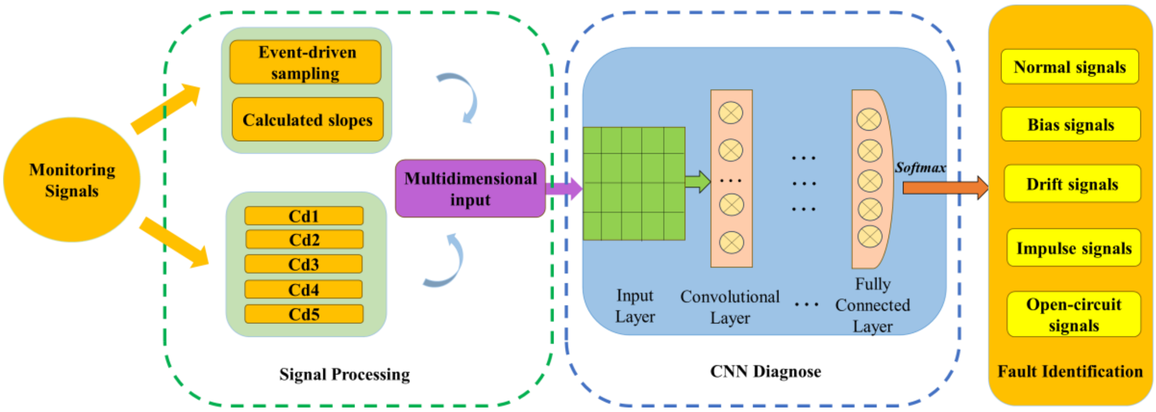

Fig. 10 Fault diagnosis model based on CNN and the multidimensional input

In the CNN, a two-layer convolutional layer structure is adopted, with the number of convolutional kernels in the first and second layers being 16 and 32, respectively. Each convolutional layer is followed by a batch normalization layer and a ReLU activation function, and spatial down-sampling is also achieved through a max pooling layer. The fully connected layer consists of two layers: the first layer contains 64 neurons and also applies the ReLU activation function, while the second layer contains 5 neurons to calculate the probabilities for each fault. Finally, the signal fault corresponding to the maximum probability is considered to be the result of the CNN model's diagnosis. During the training process, the CNN network is optimized using the cross-entropy loss function, and the Adam optimizer is used for gradient updates, with an initial learning rate set to 0.01. Additionally, the L2 regularization algorithm is also adopted to mitigate overfitting issues. After the CNN model training is completed, 55 subsamples in all signal categories are randomly shuffled and input into the trained convolutional neural network to test automatic diagnosis of the signal fault type and whether it has occurred. The diagnostic results of different signal categories are statistically analyzed, as shown in Figure 11. Meanwhile, to demonstrate the advantages of the multidimensional input, the diagnostic results based the input of raw monitoring signals and wavelet decomposition signals are provided, respectively. The diagnostic results indicate that, under the multidimensional feature signal inputs, the diagnostic model only made one misjudgment, which the CNN model misdiagnosed a bias fault as a drift fault. This misjudgment can be eliminated by extending the subsample data time. But for the input of raw monitoring signals, the number of misjudgments by the CNN diagnostic model significantly increases. The bias faults were susceptible to misclassification as either drift or impulse faults. More critically, the impulse fault signals risked being mislabeled as normal signals and consequently overlooked. Under the input of wavelet signals, the impulse signals can be also misclassified as bias signals, and there is a misclassification rate of 27.27 % that the open-circuit signals will be regarded as drift signals.

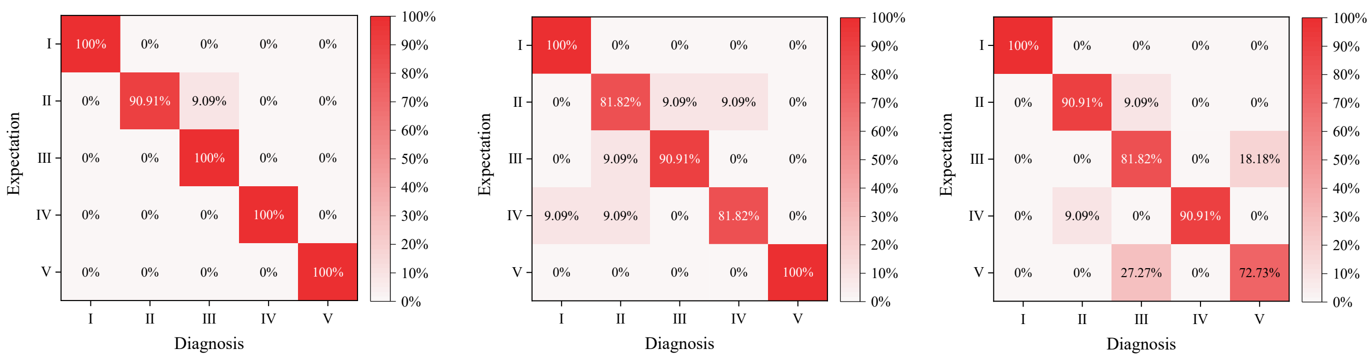

(a) Multidimensional feature signals (b) Raw signals (c) Wavelet signals

Fig. 11 Signal diagnostic results with different inputs

To better serve actual monitoring scenarios, the diagnostic accuracy metrics were categorized into three classes: missed detection rate (MDR), false alarm rate (FAR), and total diagnostic rate (TDR), as shown in Table 2. Specifically, the missed detection rate quantifies undetected fault events where the sensor fails but no alarm is triggered, while the false positive rate measures the probability of incorrect fault-type classification when an alarm occurs. The total diagnostic rate comprehensively evaluates the diagnosis model precision by jointly accounting for both missed detections and classification errors.

Table2 Comparison of fault diagnosis result in different inputs

Diagnostic indicators	Inputs of fault diagnosis model		
	Raw signals	Wavelet signals	Multidimensional feature signals
Missed detection rate (%)	1.82	0.00	0.00
False alarm rate (%)	7.27	12.73	1.82
Total diagnostic rate (%)	90.91	87.27	98.18

The statistical results demonstrate that relying solely on raw monitoring signals for fault diagnosis may lead to missed detections. Although this issue can be eliminated by performing wavelet decomposition on the signals, the complex fluctuation characteristics introduced by the wavelet analysis increase the difficulty of fault-type identification. The FAR of wavelet-based diagnosis increases by 5.46 % compared to raw signal-based methods. In contrast, the multidimensional feature signal approach demonstrates superior performance in both MDR, FAR and TDR. The multidimensional feature-based diagnosis demonstrates a 7.27 % and 10.91 % improvement in TDR compared to the raw monitoring signal and the wavelet-based methods, respectively. In fact, the multidimensional feature signals not only incorporate the wavelet components but also preserve the simplified fluctuation characteristics of the raw monitoring signals through the event-triggered sampling based on predictive zero-crossing instant. Consequently, the proposed diagnostic model can effectively prevent fault omission and maintain precise fault-type discrimination capability.

3.3 Impact of hyper-parameters on signal fault diagnosis

For artificial neural networks, the selection of hyperparameters is crucial. Therefore, the research is conducted to analyze the impact of changes in hyperparameters such as initial learning rate and ANN optimizer in the diagnosis model based on CNN. In order to comprehensively assess the model's diagnosis capability and computational efficiency, the total diagnostic rate and the number of convergence iterations are adopted as evaluation criteria. Figure 12 shows the variation of these evaluation criteria with different initial learning rates. Evidently, the initial learning rate exerts a non-negligible influence on the diagnosis model. As the initial learning rate increases, the number of convergence iterations gradually decreases and stabilizes when the initial learning rate reaches 0.1. However, the total diagnostic rate follows a different trend compared to the convergence iterations. It peaks at the initial learning rates of 0.005 and 0.01, then declines with further increases in the initial learning rate. Considering both the model efficiency and accuracy, the initial learning rate of 0.01 is selected for this diagnostic model.

The training process of CNNs is pivotal in determining the diagnostic performance for signal fault detection applications. During the model optimization phase, the network parameters, which includes the weights and biases in both convolutional and fully connected layers, undergo iterative updates to minimize the discrepancy between expected and predicted diagnostic outputs. To enhance training convergence and computational efficiency, a series of gradient descent-based optimization algorithms are typically integrated with CNN models, including Stochastic Gradient Descent with Momentum (SGDM), Root Mean Square Propagation (RMSProp), and Adaptive Moment Estimation (Adam). Figure 13 shows the variation of the CNN evaluation criteria with different ANN optimizers.

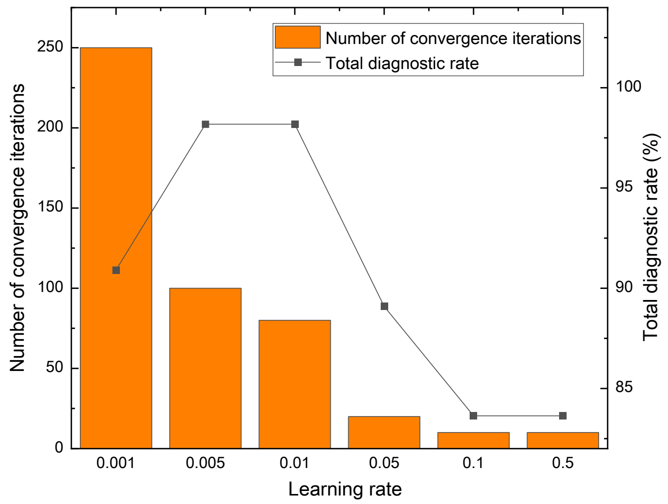

Fig. 12 Impact of initial learning rates on fault diagnosis model

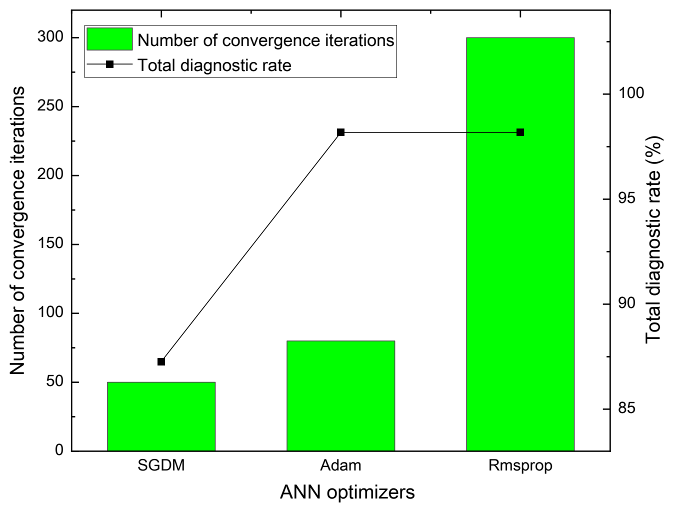

Fig. 13 Impact of ANN optimizers on fault diagnosis model

From the computational efficiency perspective, the RMSProp optimizer has the highest computational demand, requiring substantially more iterations to converge compared to other ANN optimizers. The Adam optimizer demonstrates moderate computational efficiency, while SGDM optimizer emerges as the most computationally efficient way, achieving convergence with the fewest iterations. But for total diagnostic rates, both the Adam and RMSProp-based models achieve a high-performance diagnosability. In contrast, the SGDM-optimized model shows significantly inferior identification capability, with the TDR approximately 11.11 % lower than those achieved by the Adam and RMSProp adaptive optimizations. In fact, the SGDM optimizer incorporates historical gradient information through momentum terms, which effectively accelerates convergence in consistent gradient directions while maintaining stable parameter updates. But the SGDM have some limitations in handling non-stationary optimization landscapes and may converge to suboptimal local minima. The RMSProp optimizer addresses these limitations through exponential moving averages of squared gradients, making it particularly effective for problems with sparse gradient patterns. Nevertheless, the SGDM may suffer from excessively diminished update magnitudes due to persistent accumulation of gradient squares. The Adam optimization combines the advantages of both SGDM and RMSProp methods by integrating momentum mechanisms with adaptive parameters adjustments, typically achieving superior convergence rates. Comprehensive evaluation results demonstrate that the Adam optimizer has optimal overall performance for the signal diagnosis task in this research.

3.4 Impact of signal fault severity

In actual ship structural monitoring, the signal faults have randomness not only in temporal occurrence but also in severity levels. To comprehensively evaluate the proposed model's fault identification capability and investigate its robustness, this research systematically constructs the signal faults with varying degrees of severity for the diagnosis model validation. Based on the signal fault models formulated in Table 1, this research constructs a series of fault signals with different severity levels. For bias faults, the fault intensity is systematically modulated by adjusting the bias amplitude; Regarding drift faults, the severity is controlled by varying the drift slope in a gradient manner; As for signal impulse faults, different transient characteristics are achieved by precisely regulating the impulse magnitude. It should be noted that open-circuit faults maintain inherent consistency in severity and are therefore excluded from this parametric variation investigation. The quantitative parameters used to modulate the severity levels of different signal faults are systematically summarized in Table 3.

Table3 Fault parameters for different severity levels

Fault Type	Severity of signal faults		
	Bias amplitude (MN.m)	Drift slop	Impulse magnitude (MN.m)
Bias	2.5, 2.8, 3, 5, 10, 20, 40 80, 100, 120,140,160,180	-	-
Drift	-	0.4, 0.8, 1.2, 1.8, 2.2, 3.5, 4.5	-
Impulse	-	-	4, 4.5, 5, 8, 10, 20, 40, 80, 100, 150, 180

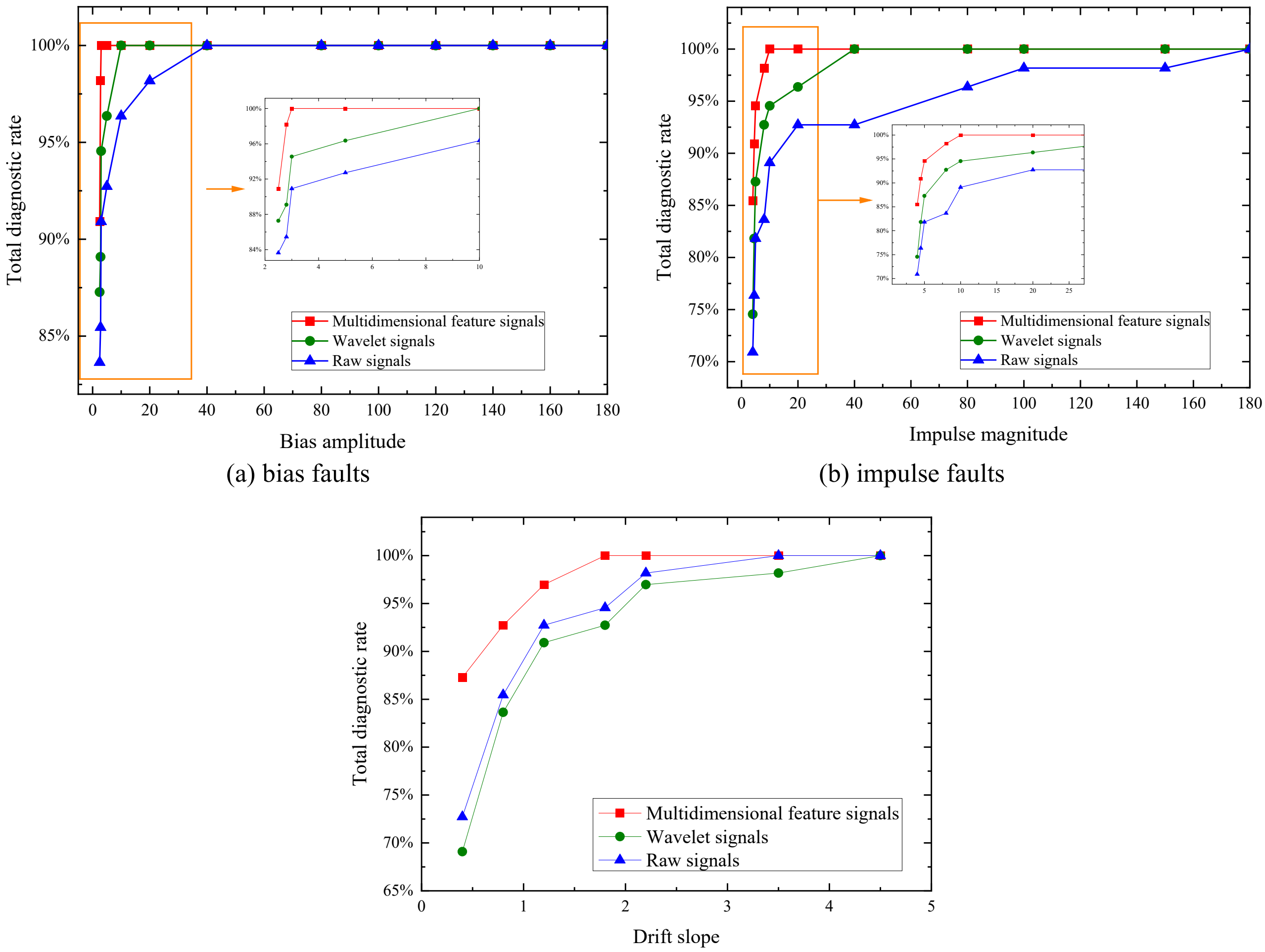

(a) bias faults (b) impulse faults

(c) drift faults

Fig. 14 Total diagnostic rates of signal faults with different fault severity levels

Figure 14 shows total diagnostic rates of signal faults with different fault severity levels. With the growth of bias amplitude, the diagnosis capabilities of these CNN models, which are based on three types of data inputs, are both gradually improved on the bias faults. The diagnosis model based on the multidimensional feature signals can catch all the simulated bias faults, whose bias amplitude is higher than 3MN·m, and its total diagnostic rate are always highest among these signal inputs. These similar superior trends are also found in impulse faults. In the identification of impulse faults, the diagnostic model ability from the wavelet signals is also enhanced significantly compared to the model ability derived from the raw monitoring signals. But for the signal drift faults, the raw signal is superior to the wavelet signals for the diagnosis model input. Although the types of signal faults are different, the multidimensional feature signals, as the input of the diagnosis model, always have advantages on the total diagnostic rates.

3.5 Impact of noise interference

Despite the fact that the monitoring data itself is perturbed by noise signals in the trimaran test, this study reconducts fault diagnosis tests after adding Gaussian noise signals to the original monitoring data to explore the impact of noise interference on the fault diagnosis model. Specifically, three levels of Gaussian noise are introduced, denoted as Added Noise I, Added Noise II, and Added Noise III, corresponding to noise intensity percentages of 5 %, 10 %, and 20 % respectively. Herein, the noise intensity percentage refers to the ratio of the noise signal amplitude to the original monitoring data amplitude, representing the relative strength of noise interference in the data. Meanwhile, to highlight the characteristics of the proposed diagnosis model, this study also employs traditional diagnostic algorithms such as Random Forest and LSTM to perform comparative diagnostic tests on the same batch of noisy monitoring data. Figure 15 shows the comparative diagnostic test with different noise levels.

In the absence of additional noise interference, the total diagnostic rates of the Random Forest-based model, the LSTM-based model, and the proposed model are 87.27 %, 90.91 %, and 98.18 % respectively. Evidently, among these diagnostic algorithms, the proposed model has the highest recognition accuracy. As the noise component expands, the total diagnostic rate based on the Random Forest algorithm shows a gradually declining trend. However, the total recognition rates of the models based on LSTM and the proposed model remain unchanged when a small amount of noise signals are added. Apparently, the Random Forest algorithm is relatively sensitive to noise interference, while the LSTM and the proposed model both have the noise resistance ability. However, the extent of this noise-resistance ability varies. For the LSTM model, false alarms start to occur when the noise intensity percentage reaches 10 %. In contrast, for the proposed model, this happens at a noise intensity percentage of 20 %. Through this comparison, it is evident that the proposed multidimensional feature-based model exhibits a higher level of noise interference resistance.

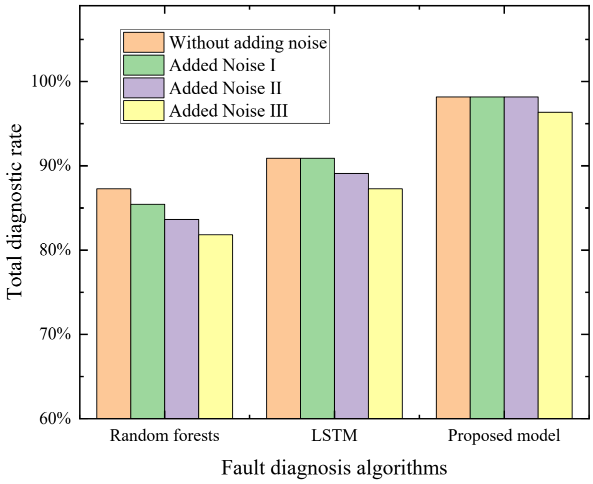

Fig. 15 Comparative diagnostic test with different noise levels

4. Verification and analysis of signal restoration

According to the results of signal fault diagnosis, the research combines the adaptive segment least squares method, predictive zero-crossing instant, and the IPSO-BP neural network to repair these fault signals. Figures 16 and 17 show the signal restoration process on the bias and drift faults, respectively. Herein, the blue curves represent the unrepaired signal, and the brown line segments represent the adaptive fitting slopes based on the predictive zero-crossing instant and the least squares algorithm. The subsequent red curves are the repaired signals after this signal restoration.

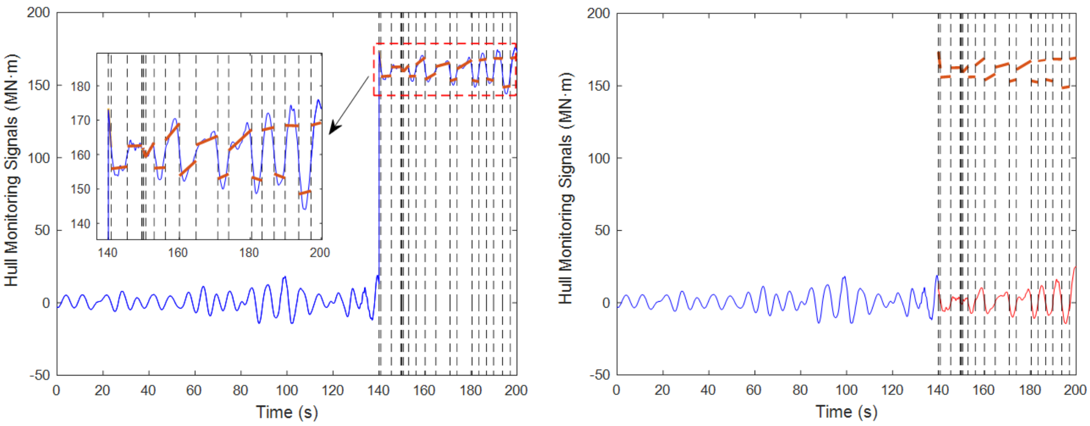

(a) adaptive fitting slopes (b) signal restoration

Fig. 16 Signal restoration process of bias faults

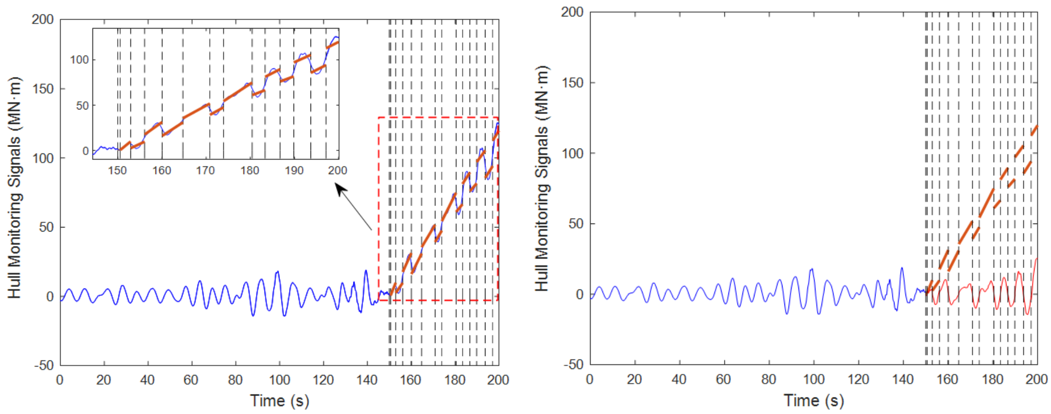

(a) adaptive fitting slopes (b) signal restoration

Fig. 17 Signal restoration process of drift faults

According to the observation of signal fluctuations before and after restoration, the adaptive segment least squares method can effectively correct deviations and drift faults, with relatively smooth transitions in signal fluctuations at restoration junctions. Figures 18 also show the signal fluctuations after restoration based on the adaptive segment least squares method and traditional mean segment least squares method, respectively. In the mean segment least squares method, the fitting slopes are calculated by evenly dividing the fluctuation of fault signal into 12 segments. It is found that traditional signal restoration has some significant mutations at the segment positions, which is weakened and become smoother in the transition by using adaptive segment least squares method. Obviously, the segment positions play a critical role on the smoothness of signal restoration, and the optimized positions based on the predictive zero-crossing instant can achieve the smooth transition in the signal restoration. The root mean square errors of these signal restorations are also calculated. For the bias faults, the RMSE of the variable segment least squares method is 1.658MN·m, which is about only a quarter of the RMSE value (6.172MN·m) obtained using the mean segment least squares method. Similarly, the RMSE of the adaptive segment least squares method on the drift faults is less than the RMSE of mean segment least squares method.

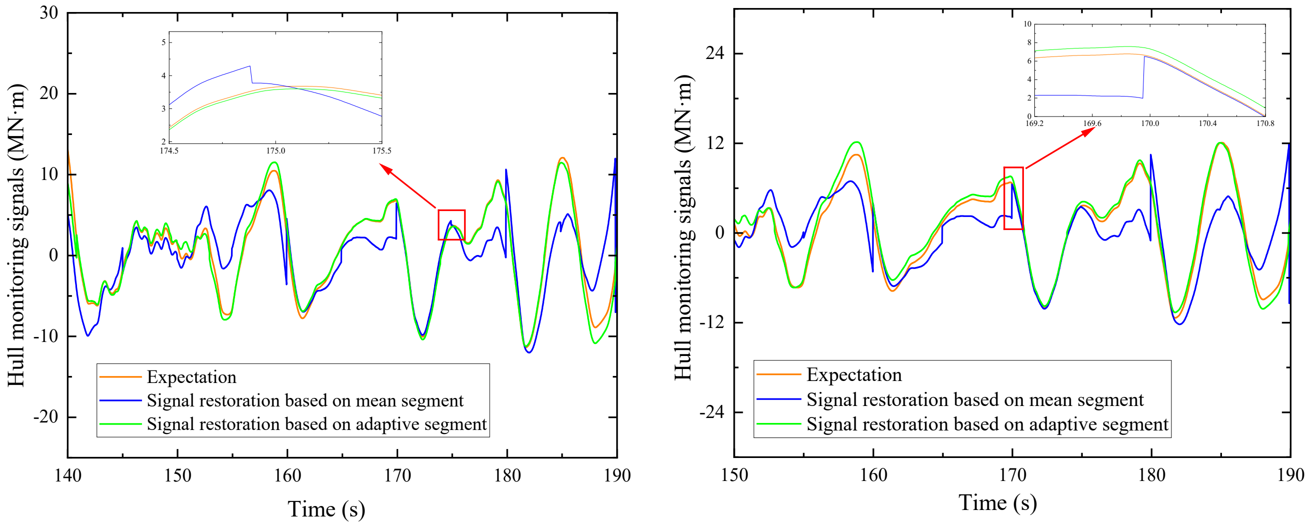

(a) signal restoration on bias faults (b) signal restoration on drift faults

Fig. 18 Comparison on signal fluctuations after restoration

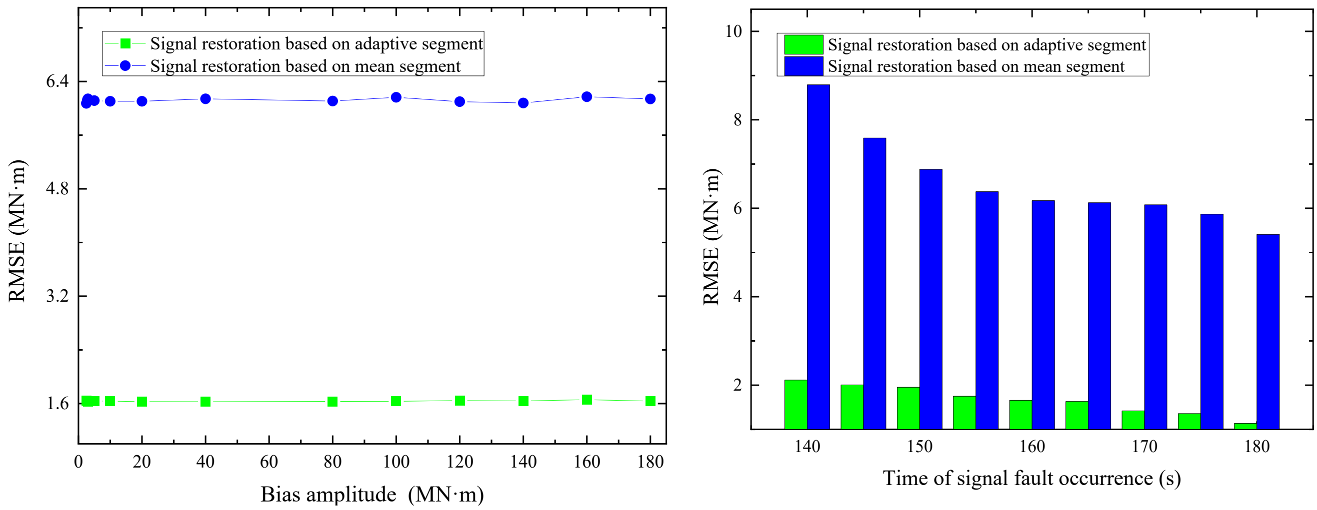

(a) impact of fault severity level (b) impact of signal occurrence time

Fig. 19 RMSE results of signal restoration on bias faults

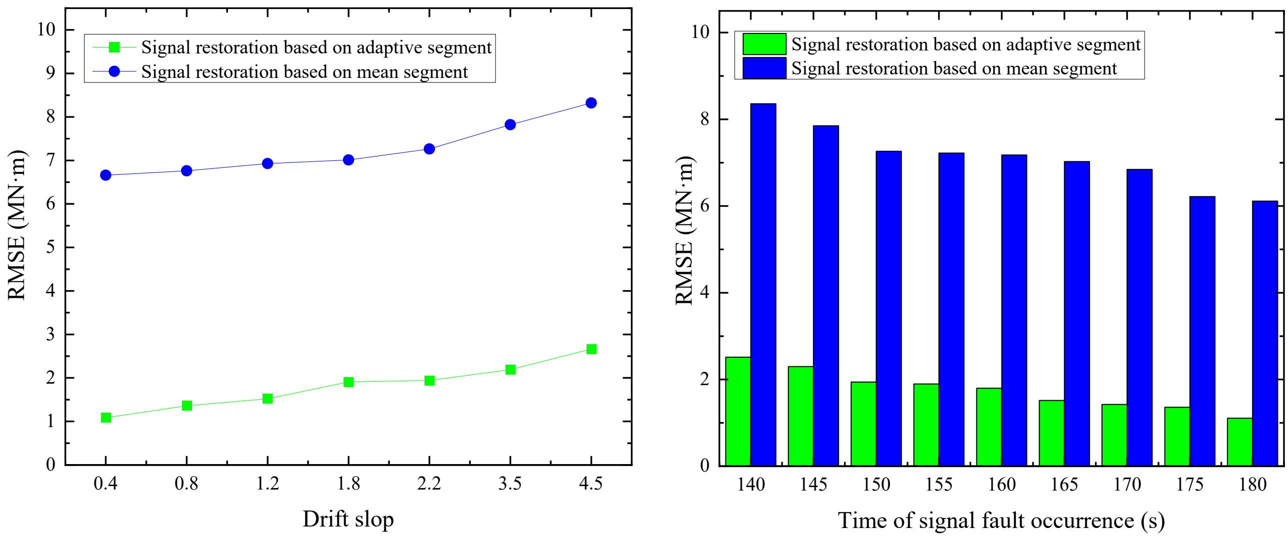

(a) impact of fault severity level (b) impact of signal occurrence time

Fig. 20 RMSE results of signal restoration on drift faults

The influences of fault occurrence time and severity on these signal restorations are investigated. Figure 19 shows the RMSE results for the signal restoration of bias faults under different fault occurrence times and fault severity levels. It is indicated that the RMSE of bias faults remains relatively stable across different deviation magnitudes, whether using the traditional mean segmentation method or the adaptive segmentation method. However, the fault occurrence time has some influence on the signal restoration of the bias faults. When the signal restoration time is short, the RMSE of bias faults decreases. Upon statistical analysis of the RMSE of the adaptive segmentation method and the traditional mean segmentation method across various occurrence times and severity levels, it becomes evident that, for bias faults, the RMSE of the adaptive segmentation approach has an average reduction of 73.86 %. Figure 20 also shows the RMSE results for the signal restoration of drift faults under varied fault occurrence times and fault severity levels. The signal restoration characteristics for drift faults differs from that of the bias faults. As the drift slope increases, the difficulty of the signal restoration on drift faults grows gradually, which raise the RMSE of drift faults. Additionally, when there is a delay in the drift fault occurrence, the RMSE of drift fault also decreases, to some extent. By calculating the RMSE of the adaptive segmentation method and the traditional mean segmentation method at different occurrence times and severity levels, it can be seen that for drift faults, the RMSE of the adaptive segmentation method is averagely reduced by 75.49 %. Apparently, the adaptive segmentation method has a relatively obvious advantage for both bias and drift faults.

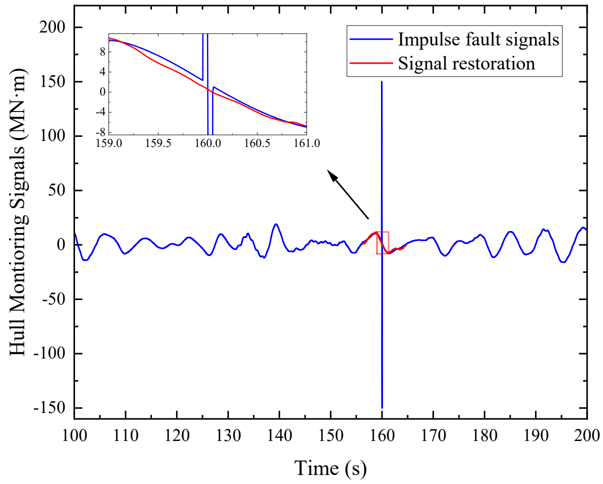

Fig. 21 Signal restoration process of impulse fault

For the impulse fault, the signal restoration is achieved by replacing the faulty impulse with the signal prediction based on the IPSO-BP neural network. Specifically, after an impact fault is diagnosed, an autonomic search for predictive zero-crossing instants is conducted around the time of its fault occurrence. Then, the signal fluctuation with the searched period, which contain the occurrence time of the impact fault, is replaced by the IPSO-BP prediction. Figure 21 shows the restoration process of the impulse fault. The predicted signal fluctuation demonstrates excellent transitional performance. The RMSE results of signal restoration with different fault occurrence times and severity levels are also summarized, as shown in Figure 22. Considering the fact that the substitution of signal fluctuation is taken in the whole searched period, the magnitude of the impulse fault basically does not affect the correction. The error in signal restoration mainly comes from the gap between the IPSO-BP prediction and actual monitoring signals in the searched period. But the occurrence time of the impulse fault has an impact on the signal restoration. For both the adaptive segmentation and mean segmentation methods, the RMSE results of impulse faults show slight fluctuations and are below 2.0. This variation in error mainly comes from the IPSO-BP prediction errors under different search periods. In addition, the RMSE of the adaptive segmentation is always higher than that of the mean segmentation. When the RMSE of the adaptive segmentation method and the traditional mean segmentation method is statistically analyzed across different occurrence times and severity levels, it is clear that, in the case of impulse faults, the RMSE of the adaptive segmentation approach is, on average, reduced by 19.55 %. The advantage of impulse signal restoration still exists in the adaptive least squares method.

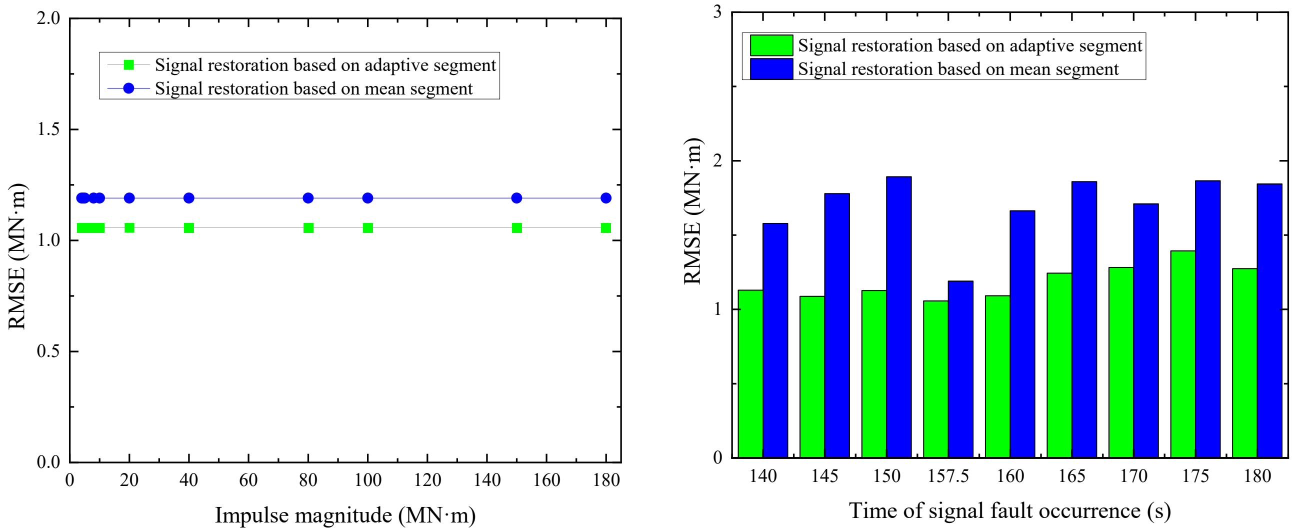

(a) impact of fault severity level (b) impact of signal occurrence time

Fig. 22 RMSE results of signal restoration on impulse faults

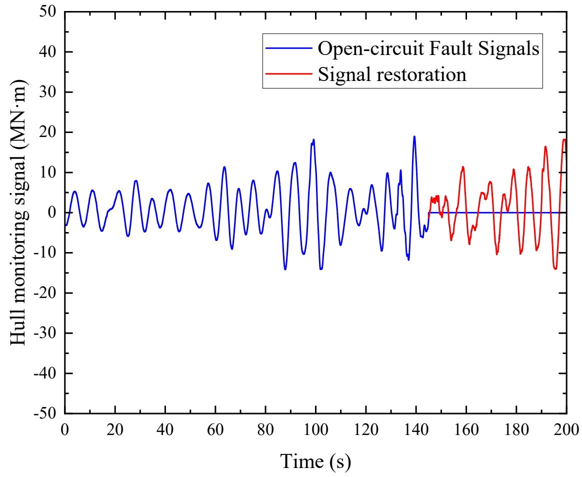

Fig. 23 Signal restoration process of open-circuit faults

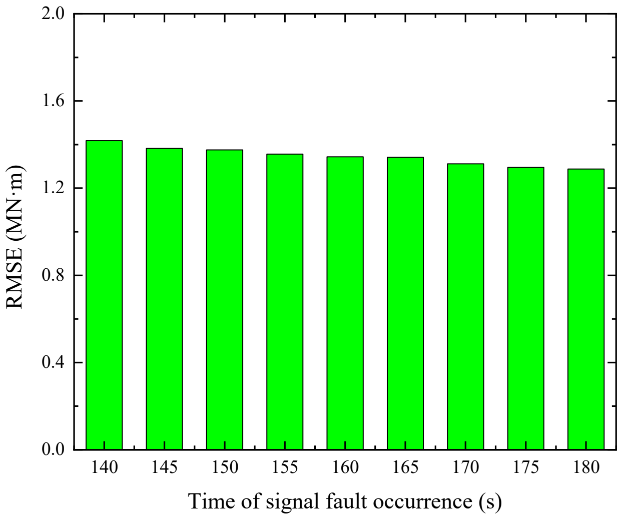

Fig. 24 RMSE results of signal restoration on open-circuit faults

For open-circuit faults, the research also adopts the similar signal compensation strategy, which use the signal fluctuation based on the IPSO-BP prediction to replace the invariable signal fault, as shown in Figure 23. Therefore, the errors in the restoration of open-circuit faults are also consistent with the prediction errors based on IPSO-BP neural network. Figure 24 show the RMSE results of signal restoration on open-circuit faults. As the occurrence time of open-circuit fault is delayed, the time period and monitoring data that need to be repaired decrease, and the RMSE results of open-circuit faults correspondingly decrease as well.

5. Signal diagnosis and restoration in different position

To verify the effectiveness of the proposed algorithm in the ship application, the monitoring signals at different monitoring positions are investigated for signal fault diagnosis and restoration. Similar to the fault diagnosis test at the stern monitoring signals (P6), the signals at the bow and midship monitoring positions (P1-P5) are also constructed with these four typical faults in the fault diagnosis testing area (120-200 s). Then, the missed detection rate, false alarm rate, and total diagnostic rate are calculated, as show in Figure 25. It is found that the signal diagnosis method has a total diagnostic rate of no less than 98 % at different ship monitoring positions, and it has more advantages in the fault diagnosis of monitoring signals at the midship (P3-P5). Although the total diagnostic rate at the bow and stern is 98.18 %, there are still occurrences of false alarm and missed detection. In fact, the monitoring signals at bow and stern always have higher high-frequency components caused by wave slamming and propeller vibration. These high-frequency signal fluctuations can mask the characteristics of the signal faults, especially when the fault severity is weak, ultimately leading to some diagnostic failure.

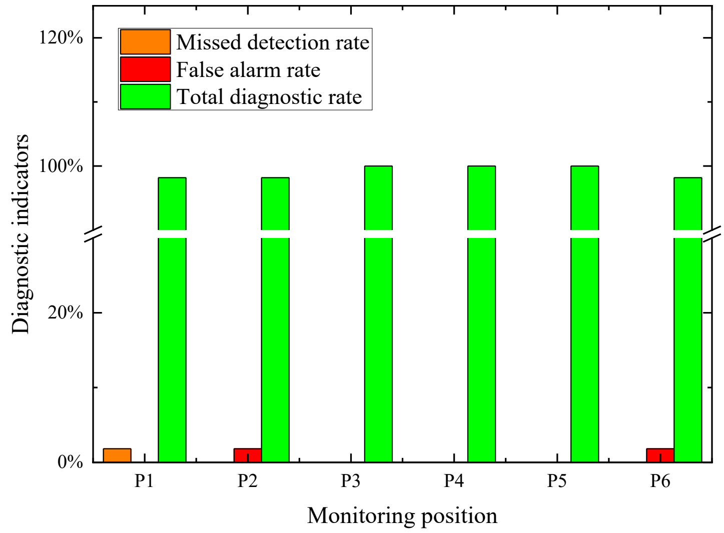

Fig. 25 Diagnostic results with different monitoring positions

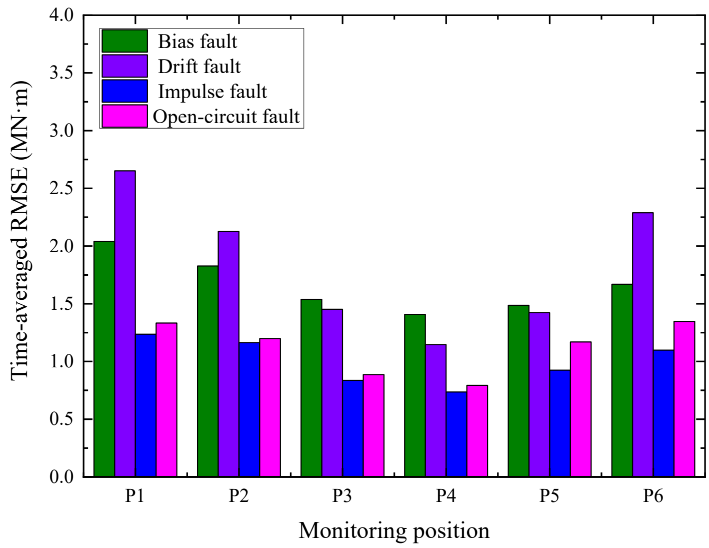

Fig. 26 Signal restoration results with different monitoring positions

After the signal diagnosis at different monitoring positions, the signal restoration is further performed on the relevant false signals, except for the diagnostic failure cases. Considering the impact of fault occurrence time on signal restoration, the time-averaged RMSE is used to characterize the accuracy of signal restoration for the same type of fault, as shown in Figure 26. It is indicated that the restoration errors for all types of signal faults are relatively higher at both bow and stern. The high-frequency fluctuation components also interfere the signal restoration, especially for the drift faults at bow. However, for the monitoring position at midship, their bias errors are more prominent and slightly higher than the drift fault errors. Due to the small restoration area, the impulse fault errors are always lowest. The distribution of the open-circuit fault error is also consistent with that of other fault errors along the ship's length. Although there are still some errors in signal fault diagnosis, the method proposed in this research has made significant improvements in the accuracy of fault diagnosis and restoration compared to traditional methods. It provides a more reliable technical support for improving the ship structure monitoring system and promotes the development of intelligent operation and maintenance for ships.

6. Conclusion

In the research, an adaptive machine learning method for signal fault diagnosis and restoration is developed to maintain the stability of structural monitoring system in intelligent ships. Four typical signal faults are analyzed and simulated, considering the characteristics of sensor failures in hull structure monitoring. The multidimensional signal feature extraction is taken by combing the wavelet transform and the event-triggered sampling based on predictive zero-crossing instants. Then, the diagnosis model based on CNN is established to achieve autonomous identification of different signal faults, and the corresponding restoration strategy is also implemented under the combination of adaptive segment least squares algorithm and IPSO-BP neural network. Finally, the following conclusions are drawn:

(1) The detailed coefficients under wavelet transform are highly sensitive to the fluctuation characteristics caused by the sensor failures. By monitoring the mutations of multi-layer detailed coefficients, the time of fault occurrence can be diagnosed effectively, which can reduce the missed detection rate in the hull structure monitoring.

(2) In the multi-signal cross-validation detection scheme, the IPSO-BP neural network can predict the signal fluctuations well at different monitoring positions. Although there is still a gap between the prediction and the actual signal fluctuations, the deviation at the zero-crossing instants is relatively small, which provides a judgment benchmark of adaptive sampling for signal diagnosis and restoration.

(3) The multidimensional input is important for the diagnosis model based on CNN. Although the signal preprocessing of wavelet analysis can reduce the missed detection rate of diagnostic models, its false alarm rate is higher than that of the diagnostic models based on raw monitoring signals. The input of the signal multidimensional feature, which combines the wavelet transform and the intelligent event-triggered sampling, has advantages on both missed detection rate, false alarm rate, and total diagnostic rate. Additionally, the proposed diagnosis always has a total diagnostic rate of no less than 98 % at different hull monitoring positions, and its noise-resistance ability is superior to that of the LSTM and Random Forest algorithms.

(4) The adaptive signal restoration strategy can effectively repair these typical signal faults. Compared with the traditional mean segmentation, it reduces RMSE by 73.86 % for bias faults, 75.49 % for drift faults, and 19.55 % for impulse faults. Furthermore, this strategy achieves smoother local connections.

The research mainly focuses on the randomness of sensor faults in terms of time and severity. The proposed method can preliminarily diagnose and repair faults occurring at different times and with different severity levels. Since the proposed algorithm has low requirements for computer performance, it can be directly installed on the actual ship's bridge for captains to use. In the actual operation of the monitoring system, regular evaluations can be carried out at fixed time intervals. For example, sensor fault diagnosis can be performed every two seconds based on the monitoring data, and then decisions on whether to carry out restoration and issue warnings can be made according to the diagnosis results. Admittedly, the current research is still in the initial stage of signal diagnosis and restoration. The signal fault characteristics in actual ship environments often present more complex scenarios, with multiple faults potentially merging. This represents the limitations of the current study. However, this research is the first step in the study of signal diagnosis and restoration systems in the field of ship structural health monitoring, laying a solid foundation for more complex fault scenarios in the future. In subsequent research, model tests in actual marine environments will be conducted. This adaptive method will be further improved by analyzing the characteristics of signal faults in actual marine environments.

ACKNOWLEDGMENTS

This research is supported by the National Natural Science Foundation of China (No.52201353), the General Program of the Natural Science Foundation of Liaoning Province (No.2025-MSLH-087), and the Fundamental Research Funds for the Central Universities (No.3132025148). All authors express their gratitude to these foundations.

REFERENCES

[1] Perera, L. P., Rodrigues, J.M., Pascoal, R., Guedes Soares, C., 2012. Development of an onboard decision support system for ship navigation under rough weather conditions. Sustainable Maritime Transportation and Exploitation of Sea Resources. *Taylor and Francis Group*, Rizzuto, E. & Guedes Soares, C., (Eds). UK, 837-844. https://doi.org/10.1201/b11810-124

[2] Jurdana, I., Ivče, R., 2014. Availability model of communication network in connecting ship systems using optical fibre technology, *Brodogradnja*, 65(03), 17-30.

[3] Trincas, G., Braidotti, L., De Francesco, L., 2017. Risk-based system to control safety level of flooded passenger ships, *Brodogradnja*, 68(01), 31-60. https://doi.org/10.21278/brod68103

[4] Hageman, R.B., Thompson, I., 2022. Virtual hull monitoring using hindcast and motion data to assess frigate-size vessel stress response. *Ocean Engineering*, 245, 110338. https://doi.org/10.1016/j.oceaneng.2021.110338

[5] Ren, H.L., Jia, L.H., Zhen C.B., Liu N., Li, J.N., 2013. Design of ship structural stress monitoring and strength assessment system. *Journal of Wuhan University of Technology*, 35(08), 60-65.

[6] Tang, H.Y., Ren, H.L., Zhong, Q., 2019. Design and model test of structural monitoring and assessment system for trimaran. *Brodogradnja*, 70(2), 111-134. https://doi.org/10.21278/brod70206

[7] Aravanis, G.I., Silionis, N.E., Anyfantis, K.N., 2023. Damage detection in ship hull structures under operational variability through strain sensing. *Ocean Engineering*, 286, 115537. https://doi.org/10.1016/j.oceaneng.2023.115537

[8] Quan, L.Q., Yuan, K.C., Zhao, H.C., 2019. Real applications of the large ship structure safety monitoring system. *Ship & Ocean Engineering*, 48(S2), 121-123.

[9] Zubaydi, A., Haddara, M.R., Swamidas, A.S.J., 2002. Damage identification in a ship's structure using neural networks. *Ocean Engineerin*g, 29(10), 1187-1200. https://doi.org/10.1016/S0029-8018(01)00077-4

[10] Muc, A., Murawski L., Szelezinski, A., 2018. Methods of cracks detection in marine structures' welded joints based on signals' time waveform analysis. *Brodogradnja*, 69(03), 43-59. https://doi.org/10.21278/brod69303

[11] Li, Y., Zhou, X.K., Li, W.H., 2024. Subsea jumper damage detection based on fractal analysis and modal characteristics. *Brodogradnja*, 75(02), 75201. https://doi.org/10.21278/brod75201

[12] Tang, H.Y., Ren, D.Y., Chen, B.Q., Guedes Soares, C., 2025. A trimaran structure damage identification method based on machine learning. *Ocean Engineering*, 320, 120315. https://doi.org/10.1016/j.oceaneng.2025.120315

[13] Frank, P.M., 1990. Fault diagnosis in dynamic systems using analytical and knowledge-based redundancy-survey and some new results. *Automatica*, 26(03), 459-474. https://doi.org/10.1016/0005-1098(90)90018-D

[14] Chojaczyk, A. A., Teixeira, A. P., Neves, L. C., Cardoso, J.B., Guedes Soares, C., 2014. Review and application of artificial neural networks models in reliability analysis of steel structures. *Structural Safety*. 52(03), 78-89. https://doi.org/10.1016/j.strusafe.2014.09.002

[15] Ding, X., Guo, L., 1998. An approach to time domain optimization of observer-based fault detection systems. *International Journal of Contro1*, 69(03), 419-442. https://doi.org/10.1080/002071798222749

[16] Tan, J., Chen, X., Cao, D., 2020. Airborne Sensor Fault Diagnosis Based on Model Parameter Identification, *Electronics Optics & Control*, 27(05), 80-84.

[17] Su, S.J., Zhe, M., Yong, Z., Song, N.Z., 2024. Digitally twin driven ship cooling pump fault monitoring system and application case. *Brodogradnja*, 75(4), 75403. https://doi.org/10.21278/brod75403

[18] Alag, S., Agogino, A.M., Morjaaria, M., 2001. A methodology for intelligent sensor measurement, validation, fusion, and fault detection for equipment monitoring and diagnostics. *Artificial intelligence for engineering design, analysis and manufacturing*, 15(4), 307-320. https://doi.org/10.1017/S0890060401154053

[19] Arık, S.Ö., Pfister, T., 2021. TabNet: Attentive interpretable tabular learning. Proceedings of the *35th AAAI Conference on Artificial Intelligence*, 2-9 February, 6679-6687. https://doi.org/10.1609/aaai.v35i8.16826

[20] Jiang, T.R., 2018. Diagnosis and prediction research of FBG sensor fault based on multi pattern recognition, Master's thesis, *Harbin Engineering University*, Harbin, China.

[21] Li, X.F., Chen, H.T., Xie, F.Q., Cao, C.H., Wang, S., Shuai, C.G., 2024. Hybrid model of multiple echo state network integrated by evidence fusion for fault diagnosis of a high-voltage circuit breaker. *IEEE Transactions on Consumer Electronics*, 70(33), 5269-5277. https://doi.org/10.1109/TCE.2024.3424280

[22] Ma, L., Zhang, F., Sun, J.Z., Fang, C., Zhang, X.Y., Xu, X.Y., 2025. Mechanical fault diagnosis of high-voltage circuit breakers based on IPSO-VMD and KFCM-SVM. *IEEJ Transactions on Electrical and Electronic Engineering*, 20(08), 1195-1202. https://doi.org/10.1002/tee.70002

[23] Huang, K. Z., Li, W. B., Gao, F., 2025. Barabási-albert model-enhanced genetic algorithm for optimizing LGBM in ship power grid fault diagnosis. *Measurement*, 249, 116954. https://doi.org/10.1016/j.measurement.2025.116954

[24] Jiao, J.L., Sun, S.Z., Ren, H.L., 2016. Predictions of wave induced ship motions and loads by large-scale model measurement at sea and numerical analysis. *Brodogradnja*, 67(02), 81-100. https://doi.org/10.21278/brod67206

[25] Jiao, J.L., Ren, H.L., Guedes Soares, C., 2021. A review of large-scale model at-sea measurements for ship hydrodynamics and structural loads. *Ocean Engineering*, 227, 108863. https://doi.org/10.1016/j.oceaneng.2021.108863

[26] Tang, H.Y., Zhu, R., Wan, Q., Ren, D.Y., 2025. Short-term prediction of trimaran load based on data driven technology. *Brodogradnja*, 76(01), 76101. https://doi.org/10.21278/brod76101

[27] Tang, H.Y., He, Z.C., Zhang, X.K., Wan, Q., 2023. Autonomous recognition of a ship structure characteristic signal based on machine learning. *International Journal of Offshore and Polar Engineering*, 33(02), 174-183. https://doi.org/10.17736/ijope.2023.mt34

[28] Tang, H.Y., Wan, Q., Ren H.L., 2023. Numerical study of trimaran wave load based on time-domain Rankine method. *Brodogradnja*, 74(3), 107-129. https://doi.org/10.21278/brod74306

[29] Jiao, J.L., Chen, Z.W., Shen, S., Jiang, C.X., Si, H.L., 2025. Ship hydroelasticity responses in long-crested irregular waves by CFD-FEM simulation in comparison with segmented model experiment. *Ocean Engineering*, 227, 120886. https://doi.org/10.1016/j.oceaneng.2025.120886

[30] Liu, L., Zhang, H., Zhang C.N., Chen J.B., Zhang B.J., Bai X.G., Song S.Y., Chen Q., Zhang W.J., 2024. Study on the effect of marine propeller wake on sediment siltation in a shallow water channel, *Brodogradnja*, 75(03), 75308. https://doi.org/10.21278/brod75308